nature physics

ARTICLES

https://doi.org/10.1038/s41567-020-0978-6

Universal scaling laws rule explosive growth in human cancers

Víctor M. Pérez-García[1]✉, Gabriel F. Calvo[1], Jesús J. Bosque[1], Odelaisy León-Triana[1], Juan Jiménez[1], Julián Pérez-Beteta[1], Juan Belmonte-Beitia[1], Manuel Valiente[2], Lucía Zhu[2], Pedro García-Gómez[2], Pilar Sánchez-Gómez[3], Esther Hernández-San Miguel[3], Rafael Hortigüela[3], Youness Azimzade[4], David Molina-García[1], Álvaro Martínez[1,5], Ángel Acosta Rojas[6], Ana Ortiz de Mendivil[7], Francois Vallette[8], Philippe Schucht[9], Michael Murek[9], María Pérez-Cano[1], David Albillo[10], Antonio F. Honguero Martínez[11], Germán A. Jiménez Londoño[12], Estanislao Arana[13] and Ana M. García Vicente[12]

Most physical and other natural systems are complex entities that are composed of a large number of interacting individual elements. It is a surprising fact that they often obey the so-called scaling laws that relate an observable quantity to a measure of the size of the system. Here, we describe the discovery of universal superlinear metabolic scaling laws in human cancers. This dependence underpins increasing tumour aggressiveness, owing to evolutionary dynamics, that leads to an explosive growth as the disease progresses. We validated this dynamic using longitudinal volumetric data of different histologies from large cohorts of patients with cancer. To explain our observations we tested complex, biologically inspired mathematical models that describe the key processes that govern tumour growth. Our models predict that the emergence of superlinear allometric scaling laws is an inherently three-dimensional phenomenon. Moreover, the scaling laws that we identified allowed us to define a set of metabolic metrics with prognostic value, which adds clinical utility to our findings.

Biological systems display complex spatially and temporally varying structures that are mainly a consequence of their underlying metabolism. Organisms continuously incorporate energetic and material resources from the environment, transforming and allocating them into different compartments that allow for their growth, reproduction and, hence, survival, both as individuals and as species. Metabolism involves random fluctuations and hierarchical processes that determine the pace at which organisms live and evolve. In a seminal work[1], it was observed that, for a broad variety of species, metabolic rates scale to the 3/4 power of the animal's mass (hereafter referred to as Kleiber's law). This result contradicted theories that assumed a direct proportionality between the volume of an animal and its metabolic rate, or other scalings, such as a proportionality to the animal's surface area. Scaling laws are of the form $Z = \alpha V^{\beta}$, where Z is an observable quantity, V is a measure of the size of the system (which, in living systems, is typically the volume or mass), α is a rate constant and β represents the scaling exponent[2]. It was proposed that the exponent $\beta = 3/4$ in Kleiber's law could be the result of principles of minimal energy[3]. Many related studies have explored allometric scaling laws in other biological contexts[4–6].

A question to ask is whether human cancers obey metabolic scaling laws. Some evidence obtained from in vitro experiments or from xenotransplantation of patient-derived cells into immunocompromised mice seems to support the idea that cancers also obey Kleiber's law or similar sublinear dynamics[7–9]. However, no works have uncovered scaling laws from large datasets of patients with cancer. Here, we address this question under the initial hypothesis that malignant tumours scale between the metabolic requirements of coordinated tissues governed by minimal energy principles (leading to an exponent $\beta \simeq 3/4$) and the metabolic requirements of independent uncoordinated units (exponent $\beta \simeq 1$).

Tumour cells exhibit high metabolic requirements to sustain an upregulated proliferation. Nutrients such as glucose and, to a lesser extent, glutamine are mostly used to fuel biomass formation and macromolecule synthesis[10]. Deregulated glucose uptake by tumour cells, known as the Warburg effect, constitutes the basis of positron-emission tomography–computed tomography (PET–CT) imaging by means of the radioactive tracer ^{18}F-fluorodeoxyglucose (^{18}F-FDG), which is widely used in clinical oncology[11]. To study the relationship between tumour metabolic rates and volume, we collected data of different cancer types imaged at diagnosis with ^{18}F-FDG PET–CT. Tumours were segmented and their total lesion activity (TLA) and metabolic tumour volume (MTV) were calculated. TLA and MTV were computed as the product of each voxel volume within the tumour with its measured standardized uptake value (SUV) and as the summed volume of the segmented tumour

[1]Mathematical Oncology Laboratory, Universidad de Castilla-La Mancha, Ciudad Real, Spain. [2]Brain Metastasis Group, Spanish National Cancer Research Centre (CNIO), Madrid, Spain. [3]Neuro-oncology Unit, Health Institute Carlos III-UFIEC, Madrid, Spain. [4]Department of Physics, University of Tehran, Tehran, Iran. [5]Department of Mathematics, Universidad de Cádiz, Cádiz, Spain. [6]Department of Radiation Oncology, Sanchinarro University Hospital, HM Hospitales, Madrid, Spain. [7]Department of Neuroradiology, Sanchinarro University Hospital, HM Hospitales, Madrid, Spain. [8]Inserm U1232, Centre de Recherche en Cancérologie et Immunologie Nantes-Angers, Nantes, France. [9]Neurosurgery Clinic, Bern Insespital, Bern, Switzerland. [10]Radiology Unit, MD Anderson Cancer Center, Madrid, Spain. [11]Thoracic Surgery Unit, Hospital General Universitario de Albacete, Albacete, Spain. [12]Nuclear Medicine Unit, Hospital General Universitario de Ciudad Real, Ciudad Real, Spain. [13]Fundación Instituto Valenciano de Oncología, Valencia, Spain.
✉e-mail: victor.perezgarcia@uclm.es

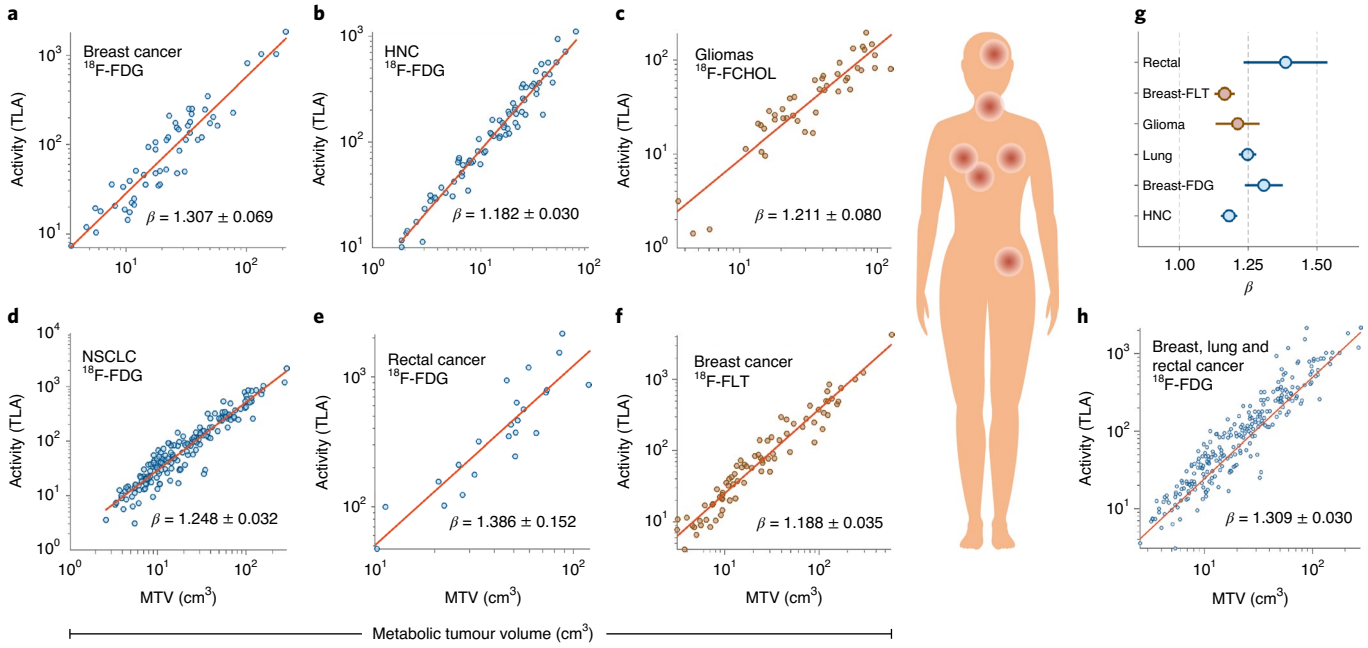

Fig. 1 | A superlinear scaling law governs glucose uptake and proliferation in human cancers. a–h, Log–log plots of TLA versus MTV for different types of cancer. ^{18}F-FDG uptake versus MTV from diagnostic PET for LABC, HNC, NSCLC and RC display superlinear ($\beta > 1$) allometric scaling laws (**a**,**b**,**d**,**e**). Diagnostic PET with proliferation radiotracers, either ^{18}F-FLT for breast cancer (**f**) or ^{18}F-FCHOL for glioma (**c**), shows the same dependence, indicating that glucose is used mostly as a resource for biosynthesis. The fitted exponents cluster around $\beta = 5/4$ (**g**). Records of patients imaged at the same institution with an identical protocol (breast-FDG, lung and rectal cancers) show that a common scaling law governs the dynamics (**h**). Error bars in (**g**) correspond to the standard error (s.d.) in the fitted parameter β obtained using fitlm.

voxels, respectively. Our first goal was to determine whether a dependence of the form TLA ~ αMTV$^{\beta}$ could be identified. Figure 1 shows log–log plots of MTV versus TLA for patients with locally advanced breast cancer (LABC), head and neck cancer (HNC, stages II–IV), non-small-cell lung cancer (NSCLC, stages I–III) and rectal cancer (RC, stages III–IV) (see Methods for more patient data). The obtained exponents were $\beta = 1.307 \pm 0.069$ ($R^2 = 0.874$, LABC), $\beta = 1.182 \pm 0.030$ ($R^2 = 0.954$, HNC), $\beta = 1.248 \pm 0.032$ ($R^2 = 0.900$, NSCLC) and $\beta = 1.386 \pm 0.152$ ($R^2 = 0.798$, RC), as shown in Fig. 1a,b,d,e. Thus, superlinear scalings cluster around the rational number $\beta = 5/4$ (Fig. 1g). Moreover, all of the patients who were scanned in the same institution under an identical protocol, and who therefore provided comparable data, followed a common scaling law with $\beta = 1.309 \pm 0.030$ ($R^2 = 0.895$) (Fig. 1h). Possible artefacts on the scaling exponents due to the partial volume effect in the PET images were discarded. Our findings contradict the hypothesis that metabolic scaling is sublinear and suggest a fundamentally different dynamic.

This superlinear glucose uptake could be the result of different mechanisms. One possibility is an increase of the Warburg phenotype, which would lead to a less efficient use of glucose. Another is the presence of immune cells and inflammation within the tumour region. However, as glucose is used mostly to satisfy the demands of cell proliferation[10,11], we suspected that an increase in the proliferation rate with size was probably the main underlying cause.

To explore this, we gathered data from patients with glioma (grades II–IV) imaged at diagnosis with ^{18}F-Fluorocholine PET (^{18}F-FCHOL), and from patients with breast cancer (stages II–IV) imaged at diagnosis with 3′-deoxy-3′-^{18}F-fluorothymidine PET (^{18}F-FLT). These two radiotracers reflect choline and thymidine metabolism and are related to cell proliferation[12,13]. The obtained scaling exponents were $\beta = 1.211 \pm 0.080$ for gliomas and $\beta = 1.188 \pm 0.035$ for breast cancers (Fig. 1c,f), which accords with a superlinear activity and provides support to the hypothesis that glucose uptake increases to satisfy the proliferation demands.

Superlinear scaling laws have been found in various systems, ranging from urban infrastructures and socioeconomic networks to primitive life forms[2]. In contrast with sublinear scaling, which leads to stable bounded growth, superlinear scaling results in unbounded growth. For biological organisms, whole-body metabolic rates increase with size across prokaryotes, protists and metazoans, although each group is characterized by a distinctive scaling relationship that is unique to their body size range[14]. In heterotrophic prokaryotes, the relationship between metabolic rate and body mass has an exponent $\beta > 1$, whereas for metazoans it is $\beta < 1$. Within an evolutionary perspective, the transition from simple prokaryotes to complex eukaryotes has shown not only a higher level of multicellular organization, but also a trend towards the 3/4 scaling exponent of Kleiber's law. Our results suggest that human cancers, as they progress, decrease the efficiency of their local vascular network[15], which would tend to increase their scaling exponents and cause them to significantly deviate from Kleiber's law.

To quantify further the relationship between tumour size and metabolism, let $B \propto V^{\beta}$ denote the metabolic rate of a tumour, where V is the volume occupied by viable cells. A simple mathematical model that accounts for energy conservation and describes the temporal dynamics of tumour growth is $B = aV + b\frac{dV}{dt}$, where the first and second terms correspond to cell maintenance and proliferation, respectively[16]. If most of the energy is used for cell biosynthesis, we may write

$$\frac{dV}{dt} = \alpha V^{\beta}. \qquad (1)$$

When $\beta > 1$, there is a finite time, $t_{crit} = t_0 + V_0^{1-\beta}/[\alpha(\beta - 1)]$, at which the tumour 'blows up', where V_0 is the volume at time t_0

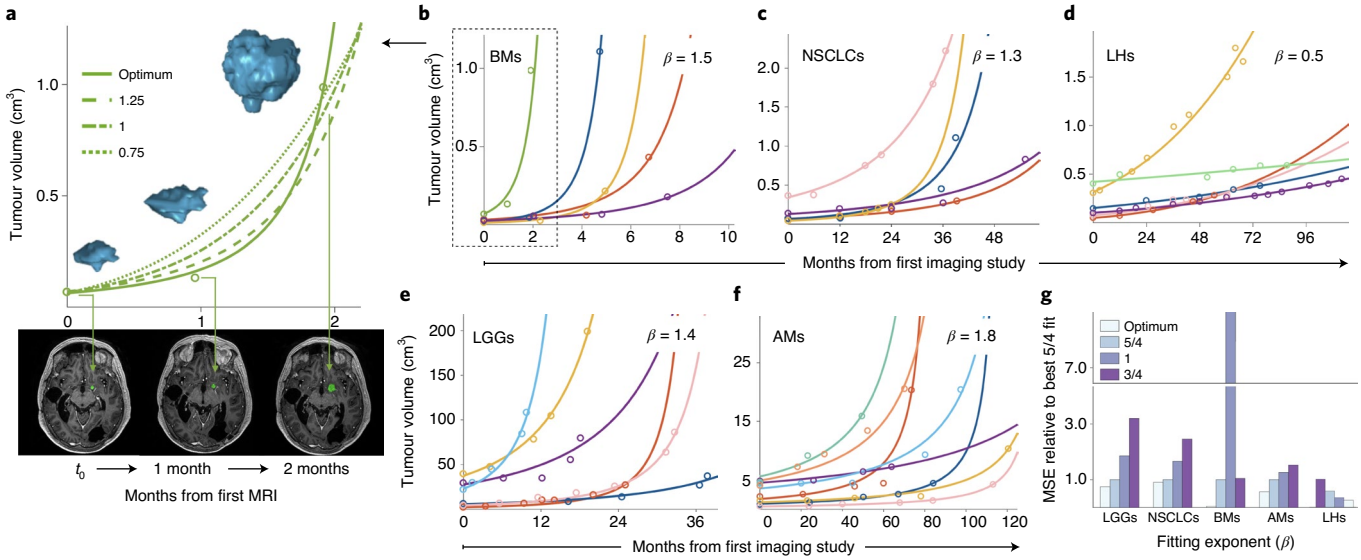

Fig. 2 | Explosive longitudinal volumetric dynamics of untreated malignant human tumours. a–g, Longitudinal volumetric data for patients with untreated brain metastases (BMs, **a**,**b**), low-grade gliomas (LGGs, **e**), NSCLCs (**c**), atypical meningiomas (AMs, **f**) and lung hamartomas (LHs, **d**). Solid curves show the fits with the optimal exponents (β values provided in each part) that give the smallest MSEs. The longitudinal three-dimensional (3D) reconstruction of a BM and representative axial slices highlighting tumour location at three time points are displayed in **a**, together with the fitting curves obtained for different exponents. MSE values for the five datasets and exponents 3/4, 1 and 5/4 (taken as a reference), in comparison with the optimal exponent, are shown in **g**. In **b**–**e**, the colours correspond to different patients.

(for details see Supplementary Information section S1. Therefore, the existence of a superlinear scaling law between proliferation and volume implies an increasingly accelerated volumetric growth and the formation of a singularity in a finite time. In real cancers such dynamics cannot be sustained to the blow-up point, as tumours are subject to physical and nutrient-supply constraints. In patients, such an accelerated growth in the final stages entails metabolic and spatial requirements that are incompatible with life.

There has long been discussion about the best mathematical model to describe tumour growth, and most models assume different types of bounded dynamics[7,17–20]. The data that support these models come from patient-derived cell lines cultured in vitro, or else from either allotransplantation of murine cells into syngeneic immunocompetent inbred mice or from xenotransplantation of patient-derived cells into immunocompromised mice. These models have a number of shortcomings compared with their human counterparts. They display a loss of genetic heterogeneity and irreversible changes in gene expression owing to long-term in vitro propagation[21], and they exhibit a rapid non-autochthonous growth that results in a perturbed tissue architecture with alterations in the vascular, lymphatic and immune compartments.

To investigate whether explosive tumour growth can observed in patients with cancer, we looked for longitudinal imaging datasets of untreated tumours. Data of this type are scarce because growing tumours are typically either treated or (as in the case of palliative care patients) not followed up with imaging. Most available datasets had either incomplete information, no volumetric imaging or very few time points. In studies of the growth dynamics of untreated WHO (World Health Organization) grade II gliomas[22], petroclival meningiomas[23], and head and neck paragangliomas[24], growth dynamics consistent with sublinear scalings were observed for slowly growing tumours. To further confirm this idea, we collected longitudinal volumetric growth data from a group of patients with lung hamartomas, the most frequent benign lung tumour type, and found a best fit to equation (1) with $\beta = 0.5 \pm 0.2$ (Fig. 2d). Hence, not all human tumours manifest an explosive growth.

We also collected imaging datasets of patients bearing tumours either that were malignant initially or that became malignant over the course of the disease (see Methods for a description of the patient datasets). The first was a set of brain metastases in which one of the lesions was either below target definition or left without therapy for medical reasons. A second set comprised initially WHO grade II gliomas that were treated with surgery and then received no other treatment for long periods. The third was from patients enrolled in a lung cancer screening programme. After detection of lung nodules with no signs of malignancy, they were followed up by low-dose CT scans. Many of these tumours had growth that accelerated up to a point at which further therapeutical actions were taken. Finally, we included a subset of petroclival meningiomas that showed signs of atypical behaviour (cases 5, 6, 9, 11 in Fig. 7 and cases 14, 18 in Fig. 8 of ref. [23]). For each patient we fitted the longitudinal volumetric growth data using different power-law models expressed by equation (1). We tested the exponents $\beta = 3/4$ (the size-limited Kleiber's law), $\beta = 1$ (an exponential growth law) and then the superlinear $\beta = 5/4$. Subsequently, we searched for the exponent that minimized the mean squared error (MSE) for all patients with each tumour type. In all of these examined cases, the existence of explosive growth dynamics was confirmed (Fig. 2b,c,e,f). A comparison of the MSEs for the different exponents and tumour types is shown in Fig. 2g. We also performed least-squares fitting of the α and β parameters for each patient and computed the mean and standard deviation for each pathology. The results obtained were 1.493 ± 0.0197 (brain metastases), 1.360 ± 0.2922 (NSCLC), 1.466 ± 0.269 (LGG) and 1.690 ± 0.452 (atypical meningiomas), respectively. Thus, exponents obtained using the two methodologies are compatible with each other and are superlinear.

To determine whether animal models can also provide evidence of superexponential tumour growth dynamics, we performed experiments on two animal models chosen because of their similarity to tumours in humans. First, we injected the human lung adenocarcinoma brain tropic model H2030-BrM (ref. [25]) into the heart of nude mice to induce the formation of brain metastasis from

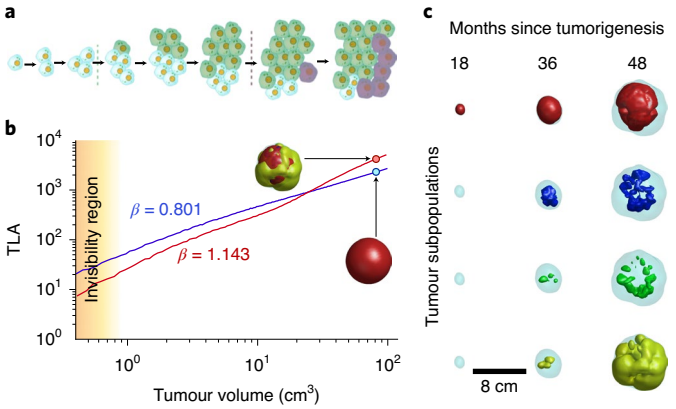

Fig. 3 | Stochastic mesoscale models with evolutionary dynamics lead to superlinear scaling laws in silico. a, Schematic representation of the evolutionary dynamics included in the mesoscale tumour growth simulator model. Random time-local discrete events that account for either mutations or phenotypic changes provide a competitive advantage to newly arising subpopulations. **b**, When a single tumour population is present, it grows continuously and displays a sublinear scaling law (blue line). By contrast, the evolutionary dynamics of a heterogeneous tumour (here, consisting of four subpopulations, see Supplementary Information section S3) yielded superlinear growth dynamics (red line). The 'invisibility region' marks the range of tumour sizes that do not give symptoms and cannot be detected by standard imaging methods. **c**, Isosurfaces of four interacting cell subpopulations at different points in time showing the dynamics of dominance by the most aggressive cells (higher indices correspond to more aggressive clones, as described by the model parameters).

systemically disseminated cancer cells. The exponent that best fit the dynamics of the brain metastasis was measured using bioluminiscence, assuming dynamics ruled by equation (1), and data from all of the mice resulted in $\beta = 1.3$. The total tumour load in the animals showed a similar behaviour, with $\beta = 1.25$ (Extended Data Fig. 1). In a second set of experiments, we injected L0627 glioma cells expressing the luciferase reporter gene into the brains of nude mice. These cells have been shown previously to recapitulate many aspects of human gliomas when injected in those animal models[26]. One month after the injection, weekly monitoring of the animals was started to measure the total flow and hence assess tumour growth. The optimal exponent obtained in this set of experiments was also $\beta = 1.25$.

Therefore, a sustained increase in proliferation is supported by both the allometric scaling laws and the morphological longitudinal growth data during the tumour's natural history. We suspected that evolutionary dynamics could be the underlying process. By genomic instability, driver gene mutations can confer to subpopulations of clonal cells somatic fitness advantages over other cells within the same tumour, and can contribute to higher proliferation rates. Mutational events are expected to occur locally in space and time. However, they require time to consolidate over the whole population[27], and thus lead to an effective continuous change in the tumour's global proliferation rate. Phenotypic variability, which manifests as trait fluctuations within identical genotypes, also leads to the further selection of cells that are by nature more proliferative[28].

The phenomenological model given by equation (1) lacks key hallmarks of real cancers. We explored in silico increasingly sophisticated spatiotemporal models that incorporate cell migration and competition among different cell subpopulations. The first mathematical model that we put forward was a non-local Fisher–Kolmogorov equation (NLFK), which encompasses random diffusive tumour cell motion and proliferation with saturation when the local carrying capacity is reached. The NLFK reads as

$$\frac{\partial u}{\partial t} = D\nabla^2 u + (\rho_0 + \rho_1 N(t))\left(1 - \frac{u}{K}\right)u \ , \qquad (2)$$

where $u = u(\mathbf{x}, t)$ denotes the tumour cell density and is a function of space $\mathbf{x}$ and time t. The model parameters are the cell diffusion constant $D > 0$, the size-independent $\rho_0 > 0$ and size-dependent $\rho_1 \geq 0$ proliferation rates and K, the local carrying capacity of the medium. The proliferation term in equation (2) includes a dependence on the total number of tumour cells $N(t) = \int u(\mathbf{x}, t)\, \mathrm{d}^3\mathbf{x}$ on the grounds that, as the total tumour size increases, there will be a higher probability of accumulated mutational events that will lead to more aggressive clones (for a derivation of the NLFK, see Supplementary Information section S2). The proliferation activity of the tumour, in the context of this model, is given by $M(t) = \mathrm{d}N/\mathrm{d}t$ and yields the scaling laws.

To quantify the effect of spatial dimensionality d on the tumour growth scaling laws, we performed a mathematical analysis of equation (2) (see Supplementary Information section S2). If $\rho_1 = 0$, the local Fisher–Kolmogorov equation is recovered, and the scaling exponent of $M(t)$ is $\beta = (d-1)/d < 1$, which results in a sublinear growth. When $\rho_1 > 0$, the proliferation activity exhibits a superlinear scaling $\beta = 2 - 2/d$, which leads to an explosive tumour growth only if $d = 3$. The tumour radial velocity, which is the rate of radial growth and a variable with prognostic value in the clinic, can also be obtained in closed form as $v_d(t) = M(t)/C_d N^{(d-1)/d}(t)$, where $C_1 = 2$ (one dimension), $C_2 = (4\pi)^{1/2}$ (two dimensions), and $C_3 = (36\pi)^{1/3}$ (three dimensions). Hence, dimensionality plays an essential role in the emergence of superlinear allometric laws within the NLFK model (equation (2)).

To further elucidate the contribution of different interacting cell subpopulations to the global tumour dynamics, we developed a stochastic mesoscale tumour growth simulator that enables cells to undergo replication, apoptosis, migration to neighbouring voxels and genotypic or phenotypic transitions (see Supplementary Information section S3). By mesoscale, we refer to a coarse-grained approach that can reach computationally clinically relevant tumour sizes (~10^2 cm^3) by working at the population level rather than that of individual cells. Extensive in silico simulations showed superlinear scaling in broad regions of the parameter space, matching both the volume range and time kinetics observed in patients (Fig. 3). Superlinear behaviour was present in so far as there was a persistent overtaking of cell subpopulations by more aggressive ones. The dynamics of uniform populations, without in silico evolutionary dynamics, displayed sublinear scalings (Fig. 3). Other mathematical models that incorporate short-range dispersal and cell turnover have reported changes in spatial growth due to the underlying evolutionary dynamics[29,30].

Scaling laws are very intriguing properties of physical and biological systems that shed light on their dynamics. They have a fundamental value but are often of limited applicability. We reasoned that, once a scaling law of the form $Z = \alpha V^{\beta}$ is set as a reference for a specific cancer type, tumours with radiotracer uptake higher than the reference level, as defined by the scaling law, would be more aggressive than those with lower levels of activity. Therefore, we computed the distance with respect to a reference scaling law (DSL) for each tumour j and dataset for which survival information was available, $\mathrm{DSL}_j = \mathrm{TLA}_j - \alpha \mathrm{MTV}_j^{\beta}$, and compared two sets with different DSL values for the whole range of values of the prefactor α, as described in Methods. Figure 4 summarizes our results for a fixed exponent $\beta = 5/4$ in four patient cohorts with distinct cancer types. We found ranges of threshold values that classify patient subpopulations into DSL groups with survival differences as measured by the Harrell's C-index.

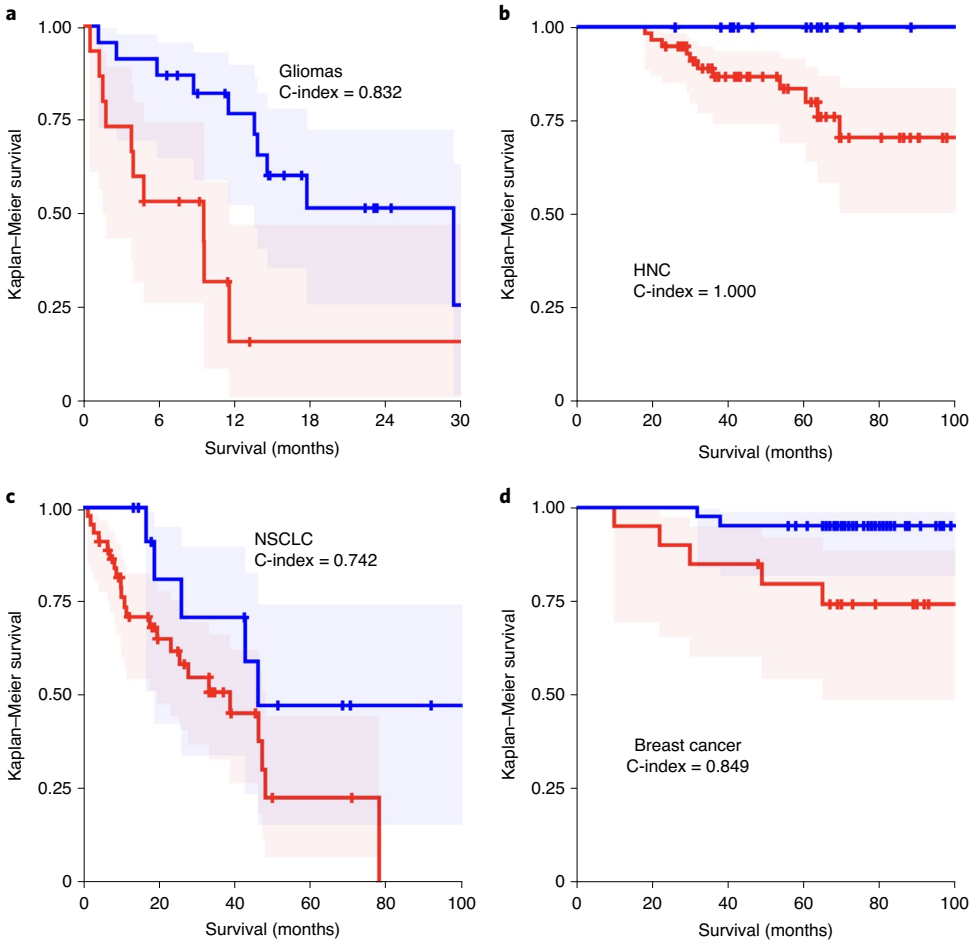

Fig. 4 | Scaling laws allow for classification of patients with cancer into prognostic groups. a–d, Patient tumours were classified as hyperactive (TLA > $\alpha V^{5/4}$; DSL > 0) or hypoactive (TLA < $\alpha V^{5/4}$; DSL < 0) using the metabolic scaling law as a reference. Survival differences between groups were compared using the Kaplan–Meier analysis and the C-index. Shown are Kaplan–Meier survival curves and the best C-index values obtained for gliomas ($P = 0.001$, C-index = 0.832, $\alpha = -0.24867$) (**a**), head and neck cancer ($P = 0.05$, C-index = 1.0, $\alpha = -0.0041776$) (**b**), stage III and IV resectable lung cancer ($P = 0.09$, C-index = 0.742, $\alpha = -0.40334$) (**c**) and breast cancer ($P = 0.019$, C-index = 0.849, $\alpha = -0.65034$) (**d**). Blue lines correspond to the survival probabilities of the group with better outcome, and red lines of the group with worse outcome. The shaded areas are confidence intervals.

The classical metabolic variables MTV and TLA classified gliomas (C-index = 1.0, $P = 0.013$ for both MTV and TLA) and breast cancer (C-index = 0.824, $P = 0.098$ for MTV; C-index = 0.87, $P = 0.01$ for TLA), but not lung cancer or head and neck cancer. Therefore, the superlinear metabolic scaling laws provided prognostic metrics that were more robust than did other classical PET-based indices.

The observation of superlinear metabolic scaling laws and explosive behaviour of malignant tumours opens up many avenues of research. Our stochastic mesoscopic framework showed how evolutionary dynamics leads to superlinearity through the competition and consolidation of different tumour subpopulations. However, evolutionary steps could be based on mutations or phenotypic variability. When an initial driver mutation appears locally in space, even when it is more advantageous, it requires some time to consolidate. During this time window, our simulations showed a continuous acceleration owing to the fact that an increasing number of cells bear this new genotype. However, once this mutation is consolidated, a plateau could develop (changing from accelerating growth to growth at a constant rate), provided no new driver mutations have appeared in the meantime. For our choice of parameters, the effective dynamics that result from our discrete simulations was in general superlinear, in agreement with our observations based on experimental data from patients and animals.

The specific mechanisms that lead to an increase in the proliferation with the tumour physical size could differ between types of cancers. Some of these mechanisms could be of evolutionary nature, related to genotype or phenotype changes (as discussed above). Alternatively, they could involve the random selection of higher fitness values[31], or they could be a consequence of acquiring driver mutations before deleterious passenger mutations[32]. Other potentially relevant processes arise in the interplay of glycolysis and tumour vascularization and oxygenation, such as the onset of the Warburg effect induced by hypoxic episodes. Others could be related to changes in the interaction between the tumour and the surrounding tissue, the action of the immune system, or alterations in the tumour microenvironment such as acidosis[33]. Some of these effects, although possibly driven by mutational alterations, in fact may be ecological in nature. Interestingly, small tumours below the spatial scale studied here may show superlinear behaviour for different reasons. Allee effect models, which originated in ecology, have shown decreased tumour growth rates at smaller tumour sizes, and these models produce growth curves that are potentially indistinguishable from superlinear growth laws when only a few data points

are fitted. Other size-related effects for small tumours may involve the interaction with the immune system: small tumours may struggle to outgrow the immune system at first, but once they reach a large enough size, the number cancer cells killed by the immune response would become negligible.

Our results emphasize the need to gain a better understanding of the evolutionary steps in different tumour histologies and to target these transformations to avoid growth acceleration. They also raise the question of whether working with experimental tumour models that show slower than superexponential growth could miss essential features of cancer dynamics. Finally, the role played by allometric scaling laws in human cancers under different therapies and the ultimate development of resistances of the tumour cells has not yet been explored.

In summary, we have found superlinear metabolic scaling laws in human cancers. These laws differ substantially from Kleiber's law, which governs the growth of many life forms, and point to accelerated growth due to underlying evolutionary dynamics that select more aggressive subpopulations. Longitudinal volumetric data from malignant tumours show explosive growth beyond classical growth-limited or exponential laws. Our mathematical models, which assume intrinsic evolutionary dynamics, put forward a mechanistic explanation for the observed phenomenology and predict that the emergence of superlinear scaling laws is an inherently three-dimensional phenomenon.

Online content

Any methods, additional references, Nature Research reporting summaries, source data, extended data, supplementary information, acknowledgements, peer review information; details of author contributions and competing interests; and statements of data and code availability are available at https://doi.org/10.1038/s41567-020-0978-6.

Received: 19 September 2019; Accepted: 25 June 2020;
Published online: 10 August 2020

References

1. Kleiber, M. Body size and metabolism. *Hilgardia* **6**, 315–351 (1932).
2. West, G. *Scale: The Universal Laws of Growth Innovation, Sustainability, and the Pace of Life in Organisms, Cities, Economies and Companies* (Penguin, 2017).
3. West, G. B., Brown, J. H. & Enquist, B. J. A general model for the origin of allometric scaling laws in biology. *Science* **276**, 122–126 (1997).
4. Savage, V. M. et al. The predominance of quarter-power scaling in biology. *Funct. Ecol.* **18**, 257–282 (2004).
5. Reich, P. B., Tjoelker, M. G., Machado, J. L. & Oleksyn, J. Universal scaling of respiratory metabolism, size and nitrogen in plants. *Nature* **439**, 457–461 (2006).
6. Enquist, B. J. et al. Biological scaling: does the exception prove the rule? *Nature* **445**, E9–10 (2007).
7. Guiot, C., Degiorgis, P. G., Delsanto, P. P., Gabriele, P. & Deisboeck, T. S. Does tumour growth follow a universal law? *J. Theor. Biol.* **225**, 147–151 (2003).
8. Herman, A. B., Savage, V. M. & West, G. B. A quantitative theory of solid tumor growth, metabolic rate and vascularization. *PLoS ONE* **6**, e22973 (2011).
9. Milotti, E., Vyshemirsky, V., Sega, M., Stella, S. & Chignola, R. Metabolic scaling in solid tumours. *Sci. Rep.* **3**, 1938 (2013).
10. Palm, W. & Thompson, C. B. Nutrient acquisition strategies in mammalian cells. *Nature* **546**, 234–242 (2017).
11. Zhu, J. & Thompson, C. B. Metabolic regulation of cell growth and proliferation. *Nat. Rev. Mol. Cell Biol.* **20**, 436–450 (2019).
12. De Grado, T. R., Reiman, R. E., Price, D. T., Wang, S. & Coleman, R. E. Pharmacokinetics and radiation dosimetry of ^{18}F-fluorocholine. *J. Nucl. Med.* **43**, 92–96 (2002).
13. Barwick, T., Bencherif, B., Mountz, J. M. & Avril, N. Molecular PET and PET/CT imaging of tumour cell proliferation using F-18 fluoro-L-thymidine: a comprehensive evaluation. *Nucl. Med. Commun.* **30**, 908–917 (2009).
14. DeLong, J. P., Okie, J. G., Moses, M. E., Sibly, R. M. & Brown, J. H. Shifts in metabolic scaling, production, and efficiency across major evolutionary transitions of life. *Proc. Natl Acad. Sci. USA* **107**, 12941–12945 (2010).
15. De Palma, M., Biziato, D. & Petrova, T. Microenvironmental regulation of tumour angiogenesis. *Nat. Rev. Cancer* **17**, 457–474 (2017).
16. West, G. B., Brown, J. H. & Enquist, B. J. A general model for ontogenetic growth. *Nature* **413**, 628–631 (2001).
17. Gerlee, P. The model muddle: in search of tumor growth laws. *Cancer Res.* **73**, 2407–2411 (2013).
18. Rodriguez-Brenes, I. A., Komarova, N. L. & Wodarz, D. Tumor growth dynamics: insights into evolutionary processes. *Trends Ecol. Evol.* **28**, 597–604 (2013).
19. Benzekry, S. et al. Classical mathematical models for description and prediction of experimental tumour growth. *PLoS Comput. Biol.* **10**, e1003800 (2014).
20. Talkington, A. & Durret, R. Estimating tumour growth rates in vivo. *Bull. Math. Biol.* **77**, 1934–1954 (2015).
21. Gengenbacher, N., Singhal, M. & Augustin, H. G. Preclinical mouse solid tumour models: status quo, challenges and perspectives. *Nat. Rev. Cancer* **17**, 751–765 (2017).
22. Mandonnet, E. et al. Continuous growth of mean tumour diameter in a subset of grade II gliomas. *Ann. Neurol.* **53**, 524–528 (2003).
23. Van Havenbergh, T., Carvalho, G., Tatagiba, M., Plets, C. & Samii, M. Natural history of petroclival meningiomas. *Neurosurgery* **52**, 55–64 (2003).
24. Heesterman, B. L. et al. Mathematical models for tumour growth and the reduction of overtreatment. *J. Neurol. Surg. B* **80**, 72–78 (2019).
25. Nguyen, D. X. et al. WNT/TCF signaling through LEF1 and HOXB9 mediates lung adenocarcinoma metastasis. *Cell* **138**, 51–62 (2009).
26. Gargini, R. et al. The IDH-TAU-EGFR triad defines the neovascular landscape of diffuse gliomas. *Sci. Transl. Med.* **12**, eaax1501 (2020).
27. Hallastschek, O. & Fisher, D. S. Acceleration of evolutionary spread by long-range dispersal. *Proc. Natl Acad. Sci. USA* **111**, E4911–E4919 (2014).
28. Deforet, M., Carmona-Fontaine, C., Korolev, K. S. & Xavier, J. B. Evolution at the edge of expanding populations. *Am. Nat.* **194**, 291–305 (2019).
29. Waclaw, B. et al. A spatial model predicts that dispersal and cell turnover limit intratumour heterogeneity. *Nature* **525**, 261–264 (2015).
30. Komarova, N. L. Spatial interactions and cooperation can change the speed of evolution of complex phenotypes. *Proc. Natl Acad. Sci. USA* **111**, 10789–10795 (2014).
31. Durrett, R., Foo, J., Leder, K., Mayberry, J. & Michor, F. Evolutionary dynamics of tumor progression with random fitness values. *Theor. Popul. Biol.* **78**, 54–66 (2010).
32. McFarland, C. D., Mirny, L. A. & Korolev, K. S. Tug-of-war between driver and passenger mutations in cancer and other adaptive processes. *Proc. Natl Acad. Sci. USA* **111**, 15138–15143 (2014).
33. Robertson-Tessi, M., Gillies, R. J., Gatenby, R. A. & Anderson, A. R. Impact of metabolic heterogeneity on tumor growth, invasion, and treatment outcomes. *Cancer Res.* **75**, 1567–1579 (2015).

Methods

Patients and image acquisition. Several patient datasets were included in our study. Data from patient subgroups 1–6 were used for the construction of the scaling laws (data from patient subgroups 1,2,4 and 5 were also used for the survival studies). Data from patient subgroups 7–10 were used for the study of the longitudinal tumour volumetric dynamics. Overall survival was determined as the time from pretreatment imaging to death or last follow-up.

Patients with breast cancer (subgroup 1). Patients were participants of a multicentre prospective study approved by the institutional review board (IRB) of Hospital General Universitario de Ciudad Real, Spain. Written informed consent was obtained from all of the patients. The inclusion criteria were (1) newly diagnosed, locally advanced breast cancer with clinical indication of neo-adjuvant chemotherapy, (2) lesion radiotracer uptake higher than background, (3) absence of distant metastases confirmed by other methods previous to the request of the PET–CT for staging, and (4) breast lesion size of at least 2 cm. In total, 54 patients were included in this dataset (18% lobular carcinoma, 82% ductal carcinoma, 100% women, age range 25–80 years, median 50 years). According to the TNM classification of malignant tumours, 54% of tumours in our dataset were T2, 18% T3, 28% T4, 28% N0, 55% N1, 6% N2, 11% N3 and 100% M0.

PET–CT examinations were performed on the same dedicated whole-body PET–CT scanner (Discovery DSTE-16s, GE Medical Systems) in three-dimensional (3D) mode. The acquisition began 60 min after intravenous administration of approximately 370 MBq (10 mCi) of ^{18}F-FDG. The image voxel size was 5.47 mm × 5.47 mm × 3.27 mm, with a slice thickness of 3.27 mm and no gaps between slices.P

Patients with head and neck cancer (subgroup 2). Data from patients with head and neck cancer were obtained from The Cancer Imaging Archive (TCIA)[34] Head-Neck-PET-CT collection (H&N1 dataset)[35]. This cohort was composed of patients with primary squamous cell carcinoma of the head and neck (stages I–IV). A total of 76 consecutive patients from this subset that satisfied the inclusion criteria (the availability of pretreatment PET studies, a well-defined primary tumour and a lesion size larger than 2 cm) were included in our study. In total, 76 patients were included in this dataset (13 cancers of the larynx, 3 hypopharynx, 11 nasopharynx, 49 oropharynx, 63 male, 13 female, age range 18–84 years, median 62 years). In terms of staging data, of the tumours, 3 were stage II, 1 stage IIB, 26 stage III, 44 stage IVA and 2 stage IVB. According to the TNM classification of malignant tumours, 14% were T1, 25% T2, 45% T3, 16% T4, 14% N0, 21% N1, 9% N2a, 36% N2b, 17% N2c, 3% N3, 95% M0 and 5% Mx.

Eligible patients had FDG-PET scans on a hybrid PET–CT scanner (Discovery ST, GE Healthcare) within 37 d before treatment (median 14 d). A median of 584 MBq (range 368–715 MBq) was injected intravenously. Imaging of the head and neck was performed using multiple bed positions with a median of 300 s (range 180–420 s) per bed position. The slice thickness resolution was 3.27 mm for all of the patients and the median in-plane resolution was 3.52 mm × 3.52 mm (range 3.52–4.69 mm^2).

Patients with rectal cancer (subgroup 3). A retrospective observational study (Scaling laws, shape factors and fractal measures in human cancers (SCALAWS)) was designed and approved by the IRB of the participating institutions. Inclusion criteria were the histological confirmation of advanced rectal cancer diagnosis, the availability of pretreatment PET–CT and a lesion size larger than 2 cm. A total of 23 patients with rectal cancer (16 male, 7 female, age range 54–80 years, median age 72 years) from the period October 2007 to October 2009 were included in the study. The PET protocol and machine were those used for subgroup 1.

Patients with lung cancer (subgroup 4). A total of 175 patients (153 men, 22 women, age range 41–84 years, median 65 years) were included in the SCALAWS study from a dataset of patients with lung cancer who underwent surgery in the period June 2007 to December 2016. Histologies were 63 squamous cell carcinomas and 112 adenocarcinomas. In terms of staging data, of the tumours, 69 were stage I, 70 stage II, 33 stage III and 3 stage IV. In terms of N staging, 107 patients had tumours classified as N0, 46 N1 and 22 N2. All of the patients had M0. The PET protocol and machine were those used for subgroup 1. We set a minimal lesion size of 2 cm as the inclusion criterion.

Patients with gliomas (subgroup 5). A prospective multicentre and non-randomized study, Functional and metabolic glioma analysis (FuMeGA), was designed and approved by the IRB of the participating institutions. Informed consent was obtained from all of the patients. Patients were included consecutively. A basal ^{18}F-FCHOL PET–CT was performed in patients suspected of having glioma after magnetic resonance imaging (MRI) with an operable brain lesion and a good Eastern Cooperative Oncology Group (ECOG) performance status (ECOG ≤ 2). Patients with a pathologically confirmed brain glioma and unifocal lesions of size larger than 2.0 cm were included. The study group included 44 patients (29 men, 15 women, age range 23–79 years, median 60 years). Histologies were 32 glioblastoma IDH1wt, 3 glioblastoma IDH1mut, 2 oligodendroglioma, 4 diffuse astrocytoma and 3 anaplastic astrocytoma.

The PET machine that was used was the same as for subgroup 1. PET acquisition was initiated 40 min after the intravenous administration of 185 MBq of ^{18}F-FCHOL. A brain scan was performed starting with a low-dose CT transmission study (modulated 120 kV and 80 mA) without intravenous contrast, followed by a 3D emission study with an acquisition time of 20 min (one single bed), voxel size of 2.3 mm × 2.3 mm × 3.3 mm in a matrix of 128 voxels × 128 voxels. The scan was then reconstructed by the application of an iterative reconstruction algorithm, using the CT images for attenuation correction.

Patients with breast cancer (subgroup 6). Pretreatment ^{18}F-FLT PET–CT scans of patients in the ACRIN 6688 observational study, available in the TCIA (ACRIN-FLT-Breast), were included in the study[36]. The dataset included a total of 75 patients (100% female, age range 22–83 years, median 50 years) with histologically confirmed breast cancer, of whom 46.8% were premenopausal and 52.2% were postmenopausal. According to the TNM classification of malignant tumours, 3% were TX, 1% T1, 47% T2, 34% T3, 14% T4, 3% NX, 29% N0, 51% N1, 11% N2, 6% N3 and 100% N0.

The inclusion criteria were (1) a primary breast cancer measuring 2 cm or more, (2) eligibility for neo-adjuvant chemotherapy and for surgical resection of the residual primary tumour after chemotherapy, and (3) no evidence of stage IV disease. Patients received a baseline pretreatment ^{18}F-FLT PET–CT study within 4 weeks before neo-adjuvant chemotherapy initiation. After the injection of 2.6 MBq kg^{-1} (mean 167 MBq; range 110–204 MBq), a whole-body image (5–7 bed positions) was obtained at 70 min (mean; range, 50–101 min).

Patients with brain metastases (subgroup 7). Patients were participants in the METMATH (Metastasis and mathematics) study, a retrospective multicentre and non-randomized study that was approved by the IRB of the participating institutions. Included in the dataset were five patients (one man, four women, age range 38–67 years, median 52 years) diagnosed with a brain metastasis of a primary lung cancer with an untreated lesion based on three or more consecutive MRI studies before treatment. Primary cancers included four NSCLC and one breast luminal b cancer. A total of 16 imaging studies were included, with 3–4 studies per patient.

The postcontrast T1-weighted sequence was a gradient echo sequence using a 3D spoiled-gradient recalled echo or a 3D fast-field echo after the intravenous administration of a single dose of gadobenate dimeglumine (0.10 mmol kg^{-1}), with a delay time of 6–8 min.

All of the MRI studies were performed in the axial plane with a 1.5 T Siemens scanner, a 3 T Philips scanner or a 1 T Philips scanner. The imaging parameters were no gap, a slice thickness of 1–1.6 mm, 0.438–0.575 mm *xy* resolutions and 0.8–1.3 mm spacing between slices.

Patients with lung cancer (subgroup 8). The patients included were participants in the SCALAMATH (scaling laws and mathematical models in cancer) study. Five patients (three men, two women, age range 60–72 years, median 68 years) were included. Three of these patients were diagnosed with adenocarcinoma and two with squamous cell carcinomas. All of the cancers were initially stage I tumours and progressed without treatment.

We drew scans from the database of follow-up screenings in the International Early Lung Cancer Action Program between 2008 and 2019, which were performed according to a common protocol[37] using low-dose CT (LDCT). Enrolment in the study was limited to those aged 50 years or older, with a smoking history of at least 10 pack-years, no previous cancer and general good health. Participants who harboured a parenchymal solid or part-solid non-calcified nodule with at least three or more follow-up CTs were identified according to criteria specified in the protocol. A total of 22 imaging studies were used, with 3–6 studies per patient.

Thoracic CT scans used a 16-acquisition-channel multidetector CT scanner (Siemens Emotion 16) with a maximum section collimation of 1 mm, 0.7 mm of spacing between slices, a slice thickness of 1 mm and a 0.584–0.783 mm range in *xy* resolutions. The CT scans were performed with 120 kVp and 30 mAs, with less than 1 s tube rotation time. Contiguous images were reconstructed in the trans-axial plane using a 1 mm thickness. Lung image sets were reconstructed with a high-frequency algorithm, and mediastinal image sets were reconstructed with an intermediate frequency algorithm.

The diagnosis of lung cancer was made by the histopathological examination of needle core biopsy or resection specimens, or by the cytopathological examination of bronchoscopic or needle aspiration biopsy samples. Resected tumours were classified based on the WHO classification of lung neoplasms. Adenocarcinomas were classified according to the classification of lung adenocarcinoma sponsored by the International Association for the Study of Lung Cancer, the American Thoracic Society and the European Respiratory Society. All of the lung cancer diagnoses were reviewed centrally. The tumours were staged using the International Association for the Study of Lung Cancer staging guidelines[37].

Patients with low-grade gliomas (subgroup 9). A total of 82 patients who were diagnosed with grade II gliomas (for whom astrocytoma, oligoastrocytoma or oligodendroglioma, according to the WHO 2007 classification, was confirmed with biopsy or surgery) and followed at the Bern University Hospital between 1990 and 2013 were initially included in the study. The study was approved by Kantonale Ethikkommission Bern.

From this patient population, we selected patients receiving either no treatment or only surgery, for whom at least five post-surgery consecutive images showing tumour growth were available. Six patients who were initially diagnosed with grade II gliomas (4 astrocytomas and 2 oligodendrogliomas, age range 29–50 years, mean 37 years) were included. A total of 34 imaging studies were used, with 4–7 studies (mean 6) per patient.

Patients with lung hamartomas (subgroup 10). Included in our study were six patients (five men, one woman, age range 51–63 years, median 58 years) who were diagnosed with lung hamartomas and who were participants of the SCALAMATH protocol with longitudinal follow-up. The imaging methods were the same as those for subgroup 8. A total of 46 imaging studies were used, with 5–12 studies (mean 8) per patient.

PET image analysis (patient subgroups 1–6). The PET scans were assessed in an Advantage Windows station (v.4) independently by an experienced nuclear medicine physician and an imaging engineer. In cases of disagreement, a third evaluator assessed the images. In the visual evaluation, a PET scan was considered to be positive if any radiotracer uptake higher than the normal tissue background was detected. Only positive PET scans were considered for tumour segmentation; that is, those that had a maximum SUV larger than twice the level of the background activity readings.

PET images in Digital Imaging and Communication in Medicine (DICOM) files were imported into the scientific software package Matlab (R2018b, The MathWorks). The tumour PET images were placed manually in a 3D box and then semi-automatically delineated using a grey-level threshold that was chosen to identify the MTV. Segmentations were corrected manually slice by slice as in ref. [38].

All of the segmentations were performed by a nuclear medicine physician and an imaging engineer, both of whom had more than 5 years of experience in tumour segmentation. In many cases, one or two additional segmentations were performed by other imaging engineers to verify the robustness of the methodology and to obtain consensus segmentations. Areas of physiological activity that were contiguous with tumour areas as defined by radiotracer uptake, such as the choroid plexus or the skull, were excluded manually from the tumour segmentations. To avoid observer-dependent biases, we developed an automatic segmentation algorithm for those tumour histologies with areas of physiological radiotracer uptake that were well separated from surrounding structures (see Supplementary Information section S5).

The radiotracer SUVs were computed for each voxel using the formula

$$\mathrm{SUV} = \frac{S_v \times R_S \times W}{R_{TD} \times D_F \times e^{\ln(2)E_t/H_F}}. \quad (3)$$

Here, S_v is the stored value, R_S is the rescaled slope, W is the patient weight, R_{TD} is the radiopharmaceutical injected dose and H_F its half-life, D_F is the decay factor, and E_t is the elapsed time for each processed slice.

We also obtained global metabolic parameters, specifically the MTV (the volume of interest after segmentation) and the TLA (the sum of all of the local SUV measures over the volume of interest). Relevant local metrics, such as the maximum value of the SUV over the segmented lesion, also were stored. Because radiotracer uptake is very low in necrotic areas, they typically do not contribute to TLA and MTV measures.

MRI image analysis (patient subgroups 7 and 9). Brain metastasis T1-weighted images were collected in DICOM format and analysed by the same image expert (O.L.-T., with 2 years of expertise in tumour segmentation) as described for patient subgroups 1–6. An experienced radiologist (E.A.) revised and validated the tumour delineation.

For subgroup 9, T2/FLAIR MRI studies were used to define the tumour volume. Radiological glioma growth was quantified by manual measurements of tumour diameters on successive MRI studies (T2/FLAIR sequences). For older imaging data that were available only as jpeg images, we used the ellipsoidal approximation[39] to compute the tumour volume.

CT image analysis (patient subgroups 8 and 10). The patients included were participants in the SCALAMATH study. CT images of lung cancer nodules were obtained in DICOM format. An experienced radiologist (E.A.) localized the lesion and then an image expert (O.L.-T.) performed the segmentations following the same methodology as for subgroups 1–7.

Glioma cells. Primary glioma cells (L0627) were kindly provided by R. Galli (San Raffaele Scientific Institute, Milan, Italy) and were grown in complete medium: a Neurobasal medium (Fisher) supplemented with B27 (1:50) (Fisher), a Glutamax medium (Fisher) (1:100), a Penicillin-streptomycin medium (Lonza) (1:100), a medium with 0.4% heparin (Sigma-Aldrich) and a medium with 40 ng ml^{-1} epidermal growth factor (EGF) and 20 ng ml^{-1} rat basic fibroblast growth factor (bFGF2; Peprotech). Cells were passaged after enzymatic disaggregation using Accumax (Milipore). To monitor tumour growth, cells were infected with lentiviral particles that expressed Fluc (pLV-Hygro-EF1A-Luciferase) (Vector-Builder) and were selected in the presence of hygromycin.

Mouse glioma xenografts. Animal care and experimental procedures were performed in accordance with the European and National guidelines for the use of animals in research and were approved by the Research Ethics and Animal Welfare Committee at the Instituto de Salud Carlos III, Madrid (PROEX 244/14). Stereotactically guided intracranial injections in athymic nude *Foxn1*^{nu} mice were performed by the administration of 1 × 105 L0627 cells (that expressed the luciferase reporter gene) resuspended in 2 µl of culture media. The injections were made into the striatum (coordinates anteroposterior from bregma, ± 0.5 mm, mediolateral from bregma, +2 mm and dorsalventral from bregma, −3 mm) using a Hamilton syringe. One month after the injection, we started to monitor the reporter expression in the tumours. In the monitoring process, animals received an intraperitoneal injection of luciferin (150 mg kg^{-1}) and the luciferase activity was visualized in an IVIS Spectrum in vivo imaging system (Perkin Elmer). The total flux (in photons per second) was measured to assess tumour growth.

Animal studies with H2030-BrM3 cells. The human lung adenocarcinoma brain tropic model H2030-BrM3 (abbreviated as H2030-BrM)[25] was injected into the hearts of nude mice to induce the formation of brain metastasis from systemically disseminated cancer cells. Brain colonization and growth of metastases were followed using non-invasive bioluminescence imaging, as BrM cells express luciferase. Upon administration of the substrate D-luciferin, bioluminescence generated by cancer cells was measured over the course of the disease. The increase in photon flux values is a well-established correlate of tumour growth in vivo[25,40]. The experiments were performed in accordance with a protocol approved by the Centro Nacional de Investigaciones Oncológicas (CNIO), the Instituto de Salud Carlos III and the Comunidad de Madrid Institutional Animal Care and Use Committee. Athymic nu/nu mice (Harlan) aged 4–6 weeks were used. Brain colonization assays were performed by the injection into the left ventricle of 100 µl of PBS containing 100,000 cancer cells. Mice anaesthetized with isofluorane were injected retro-orbitally with D-luciferin (150 mg kg^{-1}) and imaged with an IVIS Xenogen machine (Caliper Life Sciences). A bioluminescence analysis was performed using Living Image software (v.3).

Cell culture. H2030-BrM was cultured in an RPMI1640 medium supplemented with 10% FBS, 2 mM l-glutamine, 100 IU ml^{-1} penicillin-streptomycin and 1 mg ml^{-1} amphotericin B.

Statistical analysis. We performed linear regressions of the log(MTV) versus log(TLA) distributions with the Matlab (R2019a) Statistics and Machine Learning toolbox command `fitlm` to construct the scaling laws. In Fig. 2, the non-linear fittings were carried out by fixing the optimum β for all patients of the same cancer type and allowing only for the personalization of the growth parameter α. Thus, for every set of N patients with the same cancer type and with a total of M ($>3N$) data points, we fitted the N values of α. For each cancer type, the value for β that was used was the one that provided the smallest MSE. To fit the longitudinal tumour volumetric dynamics to the model (equation (1)) with different values for β ($\beta = 3/4$, 1 and 5/4) and the optimum value for β, we used the Matlab function `fmincon`.

The Harrell's C-index[41] was computed to evaluate the capacity of the model to discriminate patient subgroups with different survival time. We computed the C-index for each possible threshold α in the scaling law $\log \mathrm{TLA} = \log(\alpha) + \frac{5}{4}\log \mathrm{MTV}$ for the metabolic variables (TLA, MTV) and split the patient population into two groups (values above and below the line). Then we searched for the non-isolated significant values ($p < 0.1$) and obtained the highest value of the C-index. Kaplan–Meier curves were constructed to compare both populations and the log-rank two-tailed test was used to compute the C-index. For instances in which either no curve with $p < 0.1$ was found or the best C-index obtained was below the value 0.7, we considered the variable under study to be unable to classify patient survival outcomes accurately.

Ethical approval. We have complied with all relevant ethical regulations. Human data were obtained either from public repositories (TCIA) or as part of several retrospective or prospective observational clinical studies that were approved by the corresponding institutional review boards (for details, see Methods). Animal care and experimental procedures were performed in accordance with the European Union and national guidelines for the use of animals in research, and were reviewed and approved by the Research Ethics and Animal Welfare Committee at the Instituto de Salud Carlos III de Madrid (PROEX 244/14) (glioma cells) and in accordance with a protocol approved by the CNIO, the Instituto de Salud Carlos III and the Comunidad de Madrid Institutional Animal Care and Use Committee (H2030-BrM3 cells).

Reporting summary. Further information on research design is available in the Nature Research Reporting Summary linked to this article.

Data availability

Source data for Figs. 1,2,4 are available for this paper. All other data that support the plots within this paper and other findings of this study are available from the corresponding author upon reasonable request.

Code availability

The mesoscopic simulator code is available for download from http://matematicas.uclm.es/molab/DiscrSimulator1.zip. Source data are provided with this paper.

References

34. Clark, K. et al. The cancer imaging archive (TCIA): maintaining and operating a public information repository. *J. Dig. Imag.* **26**, 1045–1057 (2013).
35. Vallieres, M. et al. Radiomics strategies for risk assessment of tumour failure in head-and-neck cancer. *Sci. Rep.* **7**, 10117 (2017).
36. Kostakoglu, L. et al. A phase II study of 3′-Deoxy-3′-18F-Fluorothymidine PET in the assessment of early response of breast cancer to neoadjuvant chemotherapy: results from ACRIN 6688. *J. Nucl. Med.* **56**, 1681–1689 (2015).
37. Detterbeck, F. C., Boffa, D. J., Kim, A. W. & Tanoue, L. T. The eighth edition lung cancer stage classification. *Chest* **151**, 193–203 (2017).
38. Pérez-Beteta, J. et al. Tumour surface regularity at MR imaging predicts survival and response to surgery in patients with glioblastoma. *Radiology* **288**, 218–225 (2018).
39. Pallud, J. et al. Prognostic value of initial magnetic resonance imaging growth rates for World Health Organization grade II gliomas. *Ann. Neurol.* **60**, 380–383 (2006).
40. Valiente, M. et al. Serpins promote cancer cell survival and vascular co-option in brain metastasis. *Cell* **156**, 1002–1016 (2014).
41. Harrell, F. E. et al. Evaluating the yield of medical tests. *JAMA* **247**, 2543–2546 (1982).

Acknowledgements

This research has been supported by the James S. McDonnell Foundation 21st Century Science Initiative in Mathematical and Complex Systems Approaches for Brain Cancer (collaborative awards 220020560 and 220020450), Ministerio de Economía y Competitividad/FEDER, Spain (grant no. MTM2015-71200-R), Junta de Comunidades de Castilla-La Mancha (grant no. SBPLY/17/180501/000154). Research in the Brain Metastasis Group is supported by MINECO grant MINECO-Retos SAF2017-89643-R (M.V.), Bristol-Myers Squibb Melanoma Research Alliance Young Investigator Award 2017 (498103) (M.V.), Beug Foundation's Prize for Metastasis Research 2017 (M.V.), Fundación Ramón Areces (CIVP19S8163) (M.V.), Worldwide Cancer Research (19-0177) (M.V.), H2020-FETOPEN (828972) (M.V.), Fundació La Marató de tv3 (141), Clinic and Laboratory Integration Program CRI Award 2018 (54545) (M.V.), AECC Coordinated Translational Groups 2017 (GCTRA16015SEOA) (M.V.), LAB AECC 2019 (LABAE19002VALI) (M.V.), La Caixa INPhINIT Fellowship (LCF/BQ/IN17/11620028) (P.G.-G.), La Caixa-Severo Ochoa International PhD Program Fellowship (LCF/BQ/SO16/52270014) (L.Z.). M.V. is a member of the European Molecular Biology Organization Young Investigators programme (4053). We would like to acknowledge J. Cervera and J. C. Peñalver from the IVO Foundation (Valencia, Spain).

Author contributions

V.M.P.-G. designed the research, collected and processed data, performed the fittings, and developed and simulated the mathematical models. J.J.B. collected data, processed data, performed fitting tasks and developed the automatic segmentation algorithm. J.P.-B. collected and processed data. O.L.-T. collected and processed data and fitted the longitudinal volumetric data. M.V., L.Z., P.G.-G., P.S.-G., E.H.-S.M. and R.H. performed the experiments in the animal models. E.A., P.S., M.M., D.A., A.O.d.M., A.A.R., F.V. and A.F.H.M. collected data. G.A.J.L. collected and processed data. M.P.-C. processed data. G.F.C., J.J.B., J.J., J.B.-B., Y.A. and A.M. developed and simulated the mathematical models. D.M.-G. performed the survival studies. A.M.G.V. designed the research, and collected and processed data. V.M.P.-G. and G.F.C. drafted the manuscript. All of the authors edited and approved the final manuscript.

Competing interests

The authors declare no competing interests.

Additional information

Extended data is available for this paper at https://doi.org/10.1038/s41567-020-0978-6.

Supplementary information is available for this paper at https://doi.org/10.1038/s41567-020-0978-6.

Correspondence and requests for materials should be addressed to V.M.P.-G.

Reprints and permissions information is available at www.nature.com/reprints.

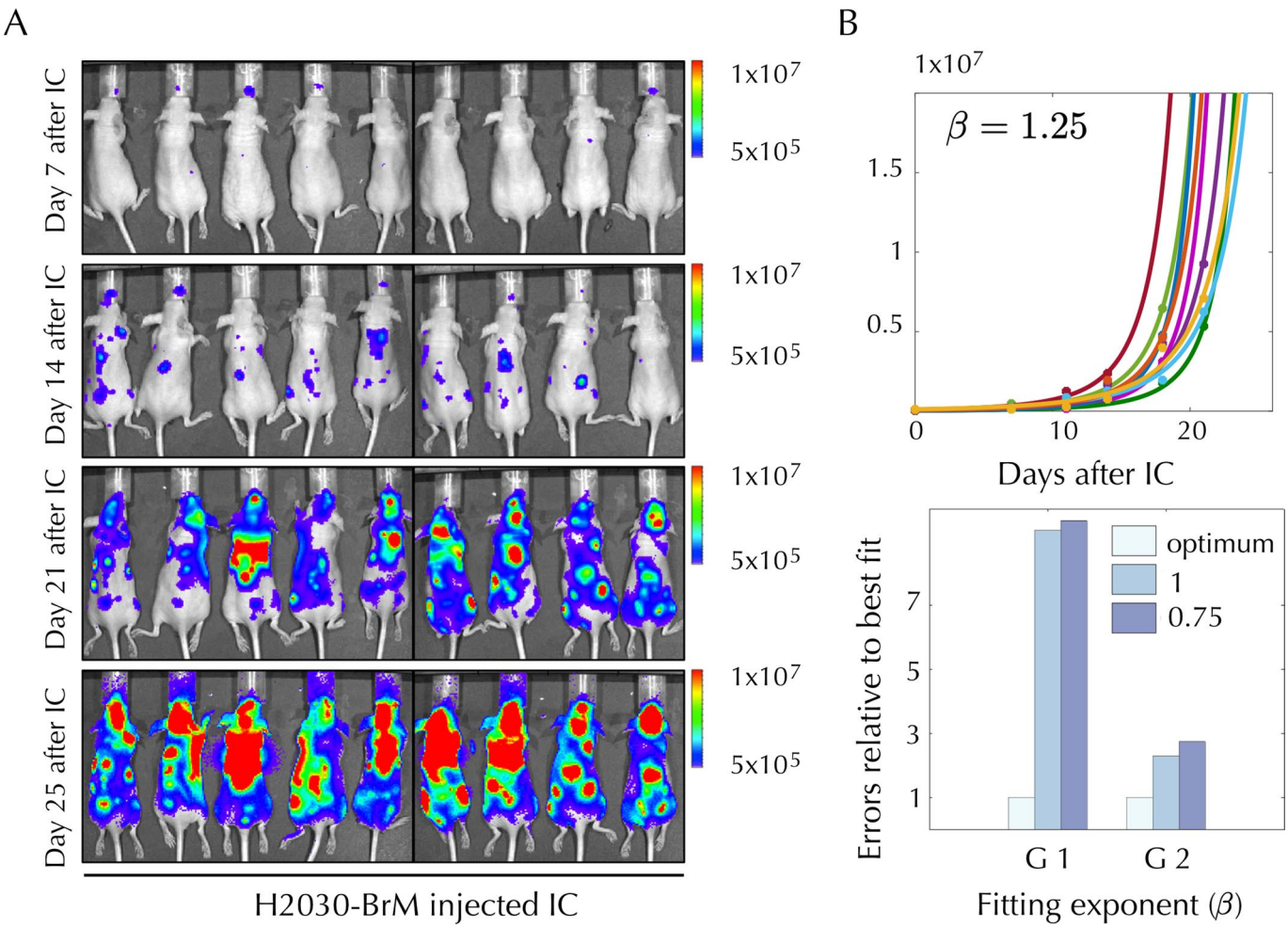

Extended Data Fig. 1 | Two human cancer animal models display superlinear growth dynamics. Two human cancer animal models display superlinear growth dynamics. Group 1 (G1) data correspond to untreated nude mice injected with the human lung adenocarcinoma brain tropic model H2030-BrM (see methods). Group data (G2) correspond to primary glioma cells (L0627) expressing the luciferase reporter gene injected into the brain of nude mice (see methods). Bioluminiscence images for G1 for some mice are shown in panel A. Total tumour mass growth curves for G1 showed superlinear dynamics with best fitting exponent $\beta = 1.25$ (for G2 it was $\beta = 1.3$). (B, upper panel). Errors relative to best fit were found to be substantially smaller with the optimal superlinear fits than for both the linear and sublinear fits (exponents 1 and 0.75 respectively) (B, lower panel).

nature research

Corresponding author(s): Víctor M. Pérez-García

Last updated by author(s): 06/08/2020

Reporting Summary

Nature Research wishes to improve the reproducibility of the work that we publish. This form provides structure for consistency and transparency in reporting. For further information on Nature Research policies, see Authors & Referees and the Editorial Policy Checklist.

Statistics

For all statistical analyses, confirm that the following items are present in the figure legend, table legend, main text, or Methods section.

n/a	Confirmed	
☐	☒	The exact sample size (*n*) for each experimental group/condition, given as a discrete number and unit of measurement
☐	☒	A statement on whether measurements were taken from distinct samples or whether the same sample was measured repeatedly
☐	☒	The statistical test(s) used AND whether they are one- or two-sided *Only common tests should be described solely by name; describe more complex techniques in the Methods section.*
☐	☒	A description of all covariates tested
☐	☒	A description of any assumptions or corrections, such as tests of normality and adjustment for multiple comparisons
☐	☒	A full description of the statistical parameters including central tendency (e.g. means) or other basic estimates (e.g. regression coefficient) AND variation (e.g. standard deviation) or associated estimates of uncertainty (e.g. confidence intervals)
☒	☐	For null hypothesis testing, the test statistic (e.g. *F*, *t*, *r*) with confidence intervals, effect sizes, degrees of freedom and *P* value noted *Give P values as exact values whenever suitable.*
☒	☐	For Bayesian analysis, information on the choice of priors and Markov chain Monte Carlo settings
☒	☐	For hierarchical and complex designs, identification of the appropriate level for tests and full reporting of outcomes
☐	☒	Estimates of effect sizes (e.g. Cohen's *d*, Pearson's *r*), indicating how they were calculated

Our web collection on statistics for biologists contains articles on many of the points above.

Software and code

Policy information about availability of computer code

Data collection	No software was used to collect the data
Data analysis	Matlab (R2018b, The Mathworks, Inc., Natick, MA, USA) was employed for all statistical analyses conducted.

For manuscripts utilizing custom algorithms or software that are central to the research but not yet described in published literature, software must be made available to editors/reviewers. We strongly encourage code deposition in a community repository (e.g. GitHub). See the Nature Research guidelines for submitting code & software for further information.

Data

Policy information about availability of data

All manuscripts must include a data availability statement. This statement should provide the following information, where applicable:

- Accession codes, unique identifiers, or web links for publicly available datasets
- A list of figures that have associated raw data
- A description of any restrictions on data availability

Source data for figures 1, 2 and 4 are available for this paper. All other data that support the plots within this paper and other findings of this study are available from the corresponding author upon reasonable request.

Field-specific reporting

Please select the one below that is the best fit for your research. If you are not sure, read the appropriate sections before making your selection.

☒ Life sciences ☐ Behavioural & social sciences ☐ Ecological, evolutionary & environmental sciences

Life sciences study design

All studies must disclose on these points even when the disclosure is negative.

Sample size	Several patient datasets were included in our study: Breast cancer (n=129), Head and Neck cancer (n=92), Rectal cancer (n=23), High-grade gliomas (n=44), Brain metastasis (n=5), Lung (n=186), Low-grade gliomas (n=82) and Hamartomas (n=5).
Data exclusions	Patients not fulfilling the inclusion criteria were excluded. The inclusion criteria were: In Breast Cancer with FDG studies, newly diagnosed locally advanced breast cancer with clinical indication of neoadjuvant chemotherapy, lesion uptake higher than background, absence of distant metastases confirmed by other methods previous to the request of the PET/CT for staging and breast lesion size of at least 2 cm and ; in Head & Neck cancer, availability of pretreatment PETstudies, presence of a well-defined primary tumour; in Rectal cancer, histological confirmation of advanced rectal cancer diagnosis and availability of pretreatment PET/CT; in High-grade gliomas, pathologically confirmed brain glioma and unifocal lesions; Breast cancer with FLT studies, primary breast cancer measuring 2.0 cm or more, being a candidate for neo-adjuvant chemotherapy and surgical resection of residual primary tumour after chemotherapy, and no evidence of stage IV disease; in Lung cancer with FDG studies, patients that received surgery were included; in Lung cancer with CT scans and temporal follow-up, enrollment was limited to those aged 50 years or older, with a smoking history of at least 10 pack-years, no previous cancer and general good health. Participants harboring parenchymal solid or part-solid non calcified nodule with at least three or more follow-up CTs were identified according to specified criteria in the protocol; in Low-grade gliomas receiving either no treatment or only surgery for which at least five post-surgery consecutive images showing tumour growth were available; in Hamartomas, longitudinal follow-up was mandatory.
Replication	Not applicable.
Randomization	Not applicable.
Blinding	Not applicable.

Reporting for specific materials, systems and methods

We require information from authors about some types of materials, experimental systems and methods used in many studies. Here, indicate whether each material, system or method listed is relevant to your study. If you are not sure if a list item applies to your research, read the appropriate section before selecting a response.

Materials & experimental systems

n/a	Involved in the study
☒	☐ Antibodies
☒	☐ Eukaryotic cell lines
☒	☐ Palaeontology
☐	☒ Animals and other organisms
☒	☐ Human research participants
☐	☒ Clinical data

Methods

n/a	Involved in the study
☒	☐ ChIP-seq
☒	☐ Flow cytometry
☐	☒ MRI-based neuroimaging

Animals and other organisms

Policy information about studies involving animals; ARRIVE guidelines recommended for reporting animal research

Laboratory animals	Two animal models were used: 1) 17 female (2-3 months old) Foxn1nu mice for glioma xenographs and 2) 37 Athymic nu/nu (Harlan) mice of 4-8 weeks of age for brain metastasis
Wild animals	Not applicable.
Field-collected samples	Not applicable
Ethics oversight	Animal care and experimental procedures were performed in accordance to the European Union and National guidelines for the use of animals in research and were reviewed and approved by the Research Ethics and Animal Welfare Committee: for animal model 1) at our institution (Instituto de Salud Carlos III, Madrid) (PROEX 244/14); for animal model 2) approved at CNIO (PROEX 211/17)

Note that full information on the approval of the study protocol must also be provided in the manuscript.

Clinical data

Policy information about clinical studies

All manuscripts should comply with the ICMJE guidelines for publication of clinical research and a completed CONSORT checklist must be included with all submissions.

Clinical trial registration	The study used data from several retrospective observational studies (not registered in any international database)
Study protocol	SCALAWS, FuMeGa, ACRIN6688 (TCIA), METMATH and SCALAMATH
Data collection	Data for SCALAWS, FuMeGa, ACRIN, METMATH and SCALAMATH studies were collected between 2007 and 2019.
Outcomes	Not applicable.

Magnetic resonance imaging

Experimental design

Design type	Retrospective.
Design specifications	Not applicable.
Behavioral performance measures	Not applicable.

Acquisition

Imaging type(s)	T1+Gd sequences.
Field strength	1, 1.5 and 3 T.
Sequence & imaging parameters	Postcontrast T1-weighted sequence was gradient echo using 3D spoiled-gradient recalled echo or 3D fast-field echo after intravenous administration of a single-dose of gadobenate dimeglumine (0.10 mmol/kg) with a (6-8)-min delay. All MRI studies were performed in the axial plane with either a 1.5 T Siemens scanner, a 3 T Philips scanner and a 1 T Philips scanner. Imaging parameters were no gap, slice thickness of 1 - 1.6 mm, 0.438-0.575 mm xy resolutions, and 0.8 - 1.3 mm spacing between slices.
Area of acquisition	Whole brain scan.

Diffusion MRI ☐ Used ☒ Not used

Preprocessing

Preprocessing software	Not applicable.
Normalization	Not applicable.
Normalization template	Not applicable.
Noise and artifact removal	Not applicable.
Volume censoring	Not applicable.

Statistical modeling & inference

Model type and settings	Not applicable.
Effect(s) tested	Not applicable.

Specify type of analysis: ☐ Whole brain ☒ ROI-based ☐ Both

Anatomical location(s): Brain.

Statistic type for inference (See Eklund et al. 2016)	Not applicable.
Correction	Not applicable.

Models & analysis

n/a	Involved in the study
☒	☐ Functional and/or effective connectivity
☒	☐ Graph analysis
☐	☒ Multivariate modeling or predictive analysis

Multivariate modeling and predictive analysis: Nonlinear regression analysis using Mean Square Errors (MSE) to fit model equations.